Space-based analysis of the cloud thermodynamic phase transition for varying microphysical and meteorological regimes

Q. Coopman[1,2,3], J. Riedi[1], S. Zeng[4], T. J. Garrett[2]

[1]Univ. Lille, CNRS, UMR 8518 - LOA - Laboratoire d'Optique Atmosphérique, Lille, France
[2]Department of Atmospheric Sciences, University of Utah, Salt Lake City, UT, USA
[3]Institute of Meteorology and Climate Research, Karlsruhe Institute of Technology, Karlsruhe, Germany
[4]NASA Langley Research Center, Hampton, VA

Key Points:

- The temperature at which liquid clouds glaciate is inferred using passive space-based instruments
- Glaciation temperature is classified by droplet radius, latitude, updraft speed, and specific humidity
- Substantially less supercooling is required for glaciation of liquid clouds composed of large droplets

Corresponding author: Quentin Coopman, quentin.coopman@kit.edu

This article has been accepted for publication and undergone full peer review but has not been through the copyediting, typesetting, pagination and proofreading process, which may lead to differences between this version and the Version of Record. Please cite this article as doi: 10.1029/2020GL087122

©2020 American Geophysical Union. All rights reserved.

Accepted Article

Abstract

Phase transitions leading to cloud glaciation occur at temperatures that vary between -38 and 0°C depending on aerosol types and concentrations, the meteorology, and cloud microphysical and macrophysical parameters, although the relationships remain poorly understood. Here, we statistically retrieve a cloud glaciation temperature from two passive space-based instruments that are part of the NASA/CNES A-Train, the POLarization and Directionality of the Earth's Reflectances (POLDER) and the MODerate-resolution Imaging Spectroradiometer (MODIS). We compare the glaciation temperature for varying bins of cloud droplet effective radius, latitude, and large-scale vertical pressure velocity and specific humidity at 700 hPa. Cloud droplet size has the strongest influence on glaciation temperature: For cloud droplets larger than 21 μm, the glaciation temperature is 6°C higher than for cloud droplets smaller than 9 μm. Stronger updrafts are also associated with lower glaciation temperatures.

1 Introduction

Between -38°C and 0°C, ice crystals and cloud droplets can coexist depending on the available water vapor and the concentration of condensation and ice nuclei [*Korolev et al.*, 2017]. Nevertheless, the phase transition of clouds from predominantly liquid to predominantly ice is still poorly understood and differences of orders of magnitude persist between theory, models, and observations [*Pruppacher*, 1995; *Jeffery and Austin*, 1997; *Cantrell and Heymsfield*, 2005]. Models tend to underestimate the fraction of liquid clouds compared with observations. One reason described by *Tan et al.* [2016] is that the Bergeron-Findeisen process is overly efficient in global climate models because mixed-phase clouds are not composed of uniformly mixed ice crystals and cloud droplets but rather pockets of pure liquid or ice.

Ice, liquid, and mixed-phase clouds have different impacts on the Earth's radiative budget through absorption and scattering of incoming solar and outgoing infrared radiation, and the influence of precipitation formation on the lifetime of clouds [*Tan et al.*, 2016]. For example, *Mülmenstädt et al.* [2015] has shown using measurements from the Cloud-Aerosol Lidar with Orthogonal Polarization (CALIOP) [*Winker et al.*, 2009] that precipitation is most frequent over mid-latitude oceans and continents when cloud tops are glaciated. Therefore, the thermodynamic cloud phase distribution is an important parameter for the determination of cloud lifetime and radiative property [*Chylek et al.*, 2006; *Matus and L'Ecuyer*, 2017].

A statistical approach based on satellite observations can be considered to understand cloud processes such as glaciation and precipitation [e.g., *Doutriaux-Boucher and Quaas*, 2004; *Quaas*, 2012; *Tapiador et al.*, 2018]. Space-based instruments offer measurements with long time-spans that are not limited to a single geographical region. Active instruments, such as CALIOP on board the Cloud-Aerosol Lidar and Infrared Pathfinder Satellite Observations satellite (CALIPSO) retrieve the vertical cloud profile of the atmosphere but mostly at cloud tops due to attenuation by thick clouds and have been used to determine cloud phase glaciation temperatures between -15°C and -25°C [*Choi et al.*, 2010; *Hu et al.*, 2010; *Komurcu et al.*, 2014]. *Cesana and Chepfer* [2013] retrieved glaciation temperatures with CALIOP from -26 to -16°C depending on different humidity bins in the upper troposphere. Active sensors are limited by the small spatial coverage due to their narrow swath which in turns can limit their statistical validity.

Passive space-based instruments have a larger spatial coverage although cloud properties such as cloud phase are only retrieved from cloud top. Methods have been developed to discriminate between liquid, ice, and mixed phase from passive satellite instruments based on differing thresholds for a range of remote sensing channels (e.g., multi-wavelength or polarization) [i.e., *Pilewskie and Twomey*, 1987; *Goloub et al.*, 2000; *Hu et al.*, 2009; *Riedi et al.*, 2010; *Baum et al.*, 2012]. *Coopman et al.* [2018] studied the cloud

©2020 American Geophysical Union. All rights reserved.

Accepted Article

phase transition in the Arctic using data from two polar orbiting satellites in the A-train, the Moderate Resolution Imaging Spectroradiometer (MODIS) and the POLarization and Directionality of the Earth's Reflectances (POLDER). For a range of cloud top heights, liquid water paths, and pollution regimes, the retrieved glaciation temperature was -17°C for cloud top pressures between 600 and 1000 hPa. It was also found that long-range pollution transport from fossil fuel combustion is associated with increases in the glaciation temperature of approximately 4°C. *Carro-Calvo et al.* [2016] statistically analyzed four years of Advanced Very-High-Resolution Radiometer (AVHRR) to show glaciation temperatures over the globe and for different seasons and cloud top altitudes to find glaciation temperatures between -20°C and -25°C in the mid-troposphere and homogeneous freezing temperature in the upper troposphere.

In the present study, we retrieve glaciation temperatures for a wide range of meteorological, dynamical, and microphysical bins globally by co-locating cloud properties derived from the passive satellites MODIS and POLDER and reanalysis data from ERA-Interim. These results are the first attempt to provide estimates of cloud glaciation temperature at global scales for varying cloud regimes.

2 Data

Cloud top properties are retrieved from a combination of two passive instruments from the A-train missions: MODIS [*Platnick et al.*, 2014] on board the Aqua satellite and POLDER-3 [*Bréon and Colzy*, 1999] on board Polarization and Anisotropy of Reflectances for Atmospheric Sciences coupled with Observation from a Lidar (PARASOL) platform. Retrieval algorithms are detailed in the above mentioned articles but we summarize hereafter only those methods used to retrieve parameters relevant to our study.

Cloud top pressure derived from POLDER-3 is based on oxygen A-Band absorption above clouds [*Buriez et al.*, 1997] whereas MODIS derives cloud top pressure from measured cloud radiative temperature and temperature profiles from ERA-Interim reanalysis [*Berrisford et al.*, 2011]. In the case of multi-layer clouds where a thin cirrus cloud overlays a liquid low level cloud, the MODIS algorithm will tend to detect ice clouds whereas the POLDER algorithm will be biaised by the lower liquid layers, potentially resulting in a warmer cloud temperature estimate [*Holz et al.*, 2008]. To avoid potential biases due to multilayer situations, we use the cloud top pressure retrievals from both sensors and discard pixels for which a significant difference is observed between the two estimates (see supplementary information for more details, Text S1 and Figures S1 and S2). Thus, multilayer and thin clouds are discarded from the dataset.

Cloud top phase is determined by an algorithm that uses a combination of shortwave, thermal infrared, and visible measurements from MODIS and multiangle polarization measurements from POLDER-3 providing a phase index (Φ) ranging from 0 to 200 [*Riedi et al.*, 2010]. *Riedi et al.* [2010] showed that the distribution of Φ can be divided in eight regimes around 20 for high confidence liquid, around 50 for confident liquid, around 80 for liquid, around 100 for mixed phase, around 120 for low confidence ice, 150 for confident ice, and 180 for high confidence ice. *Coopman et al.* [2016] showed that, for arctic clouds, Φ can be divided into three regimes ranging from 0 to 60 for liquid clouds, from 60 to 140 for clouds of unknown phase (i.e., broken clouds with unreliable phase retrievals), and from 140 to 200 for ice clouds.

Cloud effective radius (r_e) and cloud optical depth (τ) are determined from MODIS observations using a bispectral technique [*Nakajima and King*, 1990; *Platnick et al.*, 2004] that depends on the surface, viewing angle, and atmospheric state [*Platnick et al.*, 2004, 2014]. In the present study, we only consider clouds with retrieved values of τ greater than 0.3 because MODIS measurements are particularly prone to biases by surface reflectivity variability and uncertainties when clouds are optically very thin [*Platnick et al.*,

©2020 American Geophysical Union. All rights reserved.

2014]. MODIS cloud products have a spatial resolution at nadir of 1 km for cloud microphysical properties and 5 km for cloud top temperature. POLDER-3 products used in this study are obtained from the joint processing of POLDER-3/Parasol and MODIS/Aqua observation [*Riedi et al.*, 2010] and have a spatial resolution of 6 km x 6 km. MODIS cloud products are colocated to POLDER products using a nearest pixel approximation and averaged at the scale of one POLDER pixel of about 6 km×6 km.

The European Centre for Medium-Range Weather Forecasts (ECMWF) reanalysis ERA-Interim [*Berrisford et al.*, 2011] extends from 1989 to the present and was improved in 2011 [*Dee et al.*, 2011]. ERA-Interim provides meteorological parameters with a 6 hour temporal resolution at 60 pressure levels. We used the vertical pressure velocity at 700 hPa (ω_{700}) and the specific humidity at 700 hPa (SH_{700}) with a spatial resolution of 1.5°. We spatially colocate ω_{700} and SH_{700} with POLDER-MODIS measurements considering the closest pixel, and we temporally collocate by a linear interpolation between two successive ERA-I retrievals. We do not consider ω_{700} and SH_{700} as the values at the cloud levels but rather as indications of the large scale states of the atmosphere associated with the considered clouds [*Barton et al.*, 2012; *Taylor et al.*, 2015; *McDonald and Parsons*, 2018]. We spatially colocate ω_{700} and SH_{700} with POLDER-MODIS measurements considering the closest pixel and we temporally collocate by a linear interpolation between two successive ERA-I retrievals. The final dataset has a spatial resolution of 6 km×6 km.

3 Method

Algorithms used by passive sensors consider cloudy pixels to be only liquid or only ice. Considering the resolution of space-based retrievals in the kilometer range, any given cloud pixel can be a mixture of two phases leading to nonphysical cloud property temporal evolution [e.g., *Coopman et al.*, 2019]. Figure 1 shows the distribution of the phase index for data from 2005 to 2012 for all latitudes. In the present study, we assign an ad hoc uncertainty to the phase retrieval by considering two thresholds of confidence in Φ. The high confidence in Φ category considers (i) pixels with Φ between 0 and 20 as liquid and pixels with Φ between 180 and 200 as ice and the low confidence in Φ considers (ii) pixels with Φ between 0 and 60 as liquid and pixels with Φ between 140 and 200 as ice. The difference in T_{50} between (i) and (ii) is the uncertainty estimate in glaciation temperature. Pixels with Φ between 60 and 140, encompassing to 19% of the dataset are not considered in the analysis.

Figure 2-a shows the cumulative distribution function (CDF) of liquid cloud top temperature (CDF(liquide)) and 1-CDF(ice) for high and low confidence in Φ using global data. Figure 2-b shows the fraction of CDF(ice) defined as $\frac{1-CDF(ice)}{1-CDF(ice)+CDF(liq)}$ and it is associated with the ice fraction (χ_{ice}), 100% meaning all ice and 0% meaning no ice. The dataset is classified by the parameter(s) we wish to study the effect on the glaciation temperature. Doutriaux-Boucher et Quaas (2004) have shown that a hyperbolic function generally fits "very well" the relationship between χ_{ice} and cloud top temperature and it can be a surrogate model for glaciation process parametrization:

$$\chi_{ice} = \frac{1 + \tanh(-a_1 \times T + a_2)}{2} \quad (1)$$

with a_1 and a_2 fitting parameters determining respectively the flatness of the curves and the shift in temperature. The a_1 constant, units K^{-1}, controls the flatness of the curve, it is, therefore, a proxy related to the abruptness of the water-ice transition and the release of latent heat during the glaciation.. The parameter a_2 controls the shift of the curve.

From Equation (1), the temperature at which 50% of the pixels used to retrieve χ_{ice} are in the ice phase (T_{50}) is termed the glaciation temperature:

$$T_{50} = -\frac{a_2}{a_1} \quad (2)$$

©2020 American Geophysical Union. All rights reserved.

Values of a_1 and T_{50} parameters are determined for different bins of cloud droplet effective radius, latitude, large-scale ω_{700}, and SH_{700} (for details about the method, see Text S3 and Figure S3 from the supplementary information). In the present study, we refer only to T_{50} because the a_1 parameter varies weakly variable (see Text S2 in the supplementary information for more details). We do not consider a_2 as we directly refer to T_{50} to represent the shift of the curve. We defined five bins in cloud droplet effective radius, six zonal regions, six bins from ω_{700}, and five bins from SH_{700}. The different bins are defined in Table 1.

4 Results

Figure 2-c shows the values of T_{50} retrieved from five regimes: globally, over both land and sea, and for latitudes greater than 60°N and lower than 60°S. For the globe, T_{50} is equal to -24±1°C. Oceanic and land clouds each glaciate at -24±1°. Antarctic clouds glaciate at -27±1°C and Arctic ocean clouds at -23±2°C.

Figure 3 shows T_{50} as a function of r_e^{Liq}. T_{50} increases with r_e^{Liq} from -27°C for r_e^{Liq} in a bin between 5 and 9 μm to -20°C for r_e^{Liq} in a bin between 21 and 25 μm using global data considering Φ from 0 to 20 for liquid clouds and from 180 to 200 for ice clouds. Considering Φ from 0 to 60 for liquid clouds and from 140 to 200 for ice clouds, T_{50} increases from -25°C for r_e^{Liq} in a bin between 5 and 9 μm to -20°C for r_e^{Liq} in a bin between 21 and 25 μm.

In order to isolate the relationship between glaciation temperature and latitude, 700 hPa pressure velocity (ω_{700}), and specific humidity at 700 hPa (SH_{700}), we further bin according to three bins of r_e^{Liq} with thresholds at 5, 9, 13, and 17 μm containing 74% (1.8×10^9 pixels) of the total cloudy pixels. Figures 4-a, -b, and -c show T_{50} as a function of latitude band for different bins of r_e^{Liq}. In each of the three r_e bins, T_{50} is the highest for the latitude bin between 30°S and 0°N with values ranging from -17 to -16°C. Figures 4-d, -e, and -f show T_{50} as a function of large scale ω_{700}. T_{50} increases with ω_{700} ranging from -31±1°C for ω_{700} large-scale ascent between -1 and -0.8 Pa/s to -24±1°C for ω_{700} descent and for r_e^{Liq} between 5 and 9 μm. Figures 4-g, -h, and -i show that small values of cloud effective radius are associated with T_{50} correlating with specific humidity SH_{700}: For effective radii between 5 and 9 μm, T_{50} increases from -25±1°C for SH_{700} between 0.6 and 1.1 g/kg to -23±1°C for SH_{700} between 2.5 and 15.6 g/kg; for effective radii between 13 and 17 μm, T_{50} increases from -20±1°C for SH_{700} between 0.6 and 1.1 g/kg to -22±1°C for SH_{700} between 2.5 and 15.6 g/kg.

5 Discussion and Conclusion

We used 8.5 years of observations retrieved by the passive instruments POLDER-3 and MODIS to analyse retrieved liquid and ice cloud temperature distributions at a global scale. From cloud-top temperature distributions, we determine the glaciation temperature T_{50} for which 50% of the pixels are in the ice and liquid phase. Globally, T_{50} is on average equal to -24±1°C, both oceanic and land clouds glaciate at -24±1°C. Antarctic and arctic clouds glaciates at -27±1°C and -23±1°C respectively. It should be noted that the mean r_e^{liq} is equal to 11.5μm considering high confidence in Φ and 13.1μm considering low confidence in Φ, cloud droplets with an effective radius between 5 and 13 μm represent 62% of the dataset (see Figure S4 in the supplementary material for more information). Therefore, the global T_{50} is significantly driven by the behavior of small cloud droplets.

We sub-divided the global dataset into five bins of cloud droplet effective radius, six bins of latitude, and five bins of pressure velocity at 700 hPa (ω_{700}) and specific humidity at 700 hPa (SH_{700}) to represent the large scale state of the atmosphere. The strongest signal we observe is that large cloud droplet effective radii r_e^{Liq} are associated with sig-

©2020 American Geophysical Union. All rights reserved.

nificantly higher values of T_{50}. T_{50} increases from -26±1°C for r_e^{Liq} in a bin between 5 and 9 μm to -20±1°C for r_e^{Liq} in a bin between 21 and 25 μm. Higher values of r_e^{Liq} are associated with higher T_{50} in line with previous studies [e.g., *Rangno and Hobbs*, 2001; *Rosenfeld et al.*, 2011; *Coopman et al.*, 2018]. We further classified the data by r_e^{Liq} to retrieve T_{50} binned according to latitude, ω_{700}, and SH_{700}. T_{50} is a maximum in the tropical latitude band between -30° and 0°. The largest latitudinal variations in T_{50} are found for r_e^{Liq} in a bin between 5 and 9 μm between the latitude bins 60-90°S and 30-0°S. The latitudinal variation of T_{50} has been described by *Carro-Calvo et al.* [2016] with passive space-based instruments and *Cesana et al.* [2015] using models, active space-based instruments, and reanalysis data. Both studies are in line with our observations showing higher glaciation temperatures in the sub-tropic regions than in the middle and high-latitudes. Also, higher large-scale ascent is associated with lower T_{50}. For example, for r_e^{Liq} in a bin between 5 and 9 μm, T_{50} increases from -31°C for upwelling between -1 and -0.8 Pa/s to -24°C for downwelling.

These results are based on satellite observations, therefore we can only hypothesize the causes of the different correlations observed. It is possible that antarctic clouds glaciate at lower temperature than other clouds because antarctic clouds are in contact with lower concentrations of aerosols that may serve as potential ice nuclei and facilitate phase transitions. *Coopman et al.* [2018] studied the phase transition of arctic clouds for different regimes of pollution from fossil fuel combustion and retrieve a glaciation temperature of about -20°C, the presence of pollution increases the glaciation temperature up to 4°C. Similarly, *Filioglou et al.* [2019] have shown from CALIPSO and CloudSat measurements that high aerosol loadings increase the glaciation temperature by 10°C in presence of dust and continental aerosols in the Arctic. We suggest that larger liquid cloud droplets are associated with higher glaciation temperatures because they aid secondary ice nucleation [*Rosenfeld et al.*, 2011]. Small droplets do not support drizzle formation and riming and cannot be associated with ice splinter production [*Rangno and Hobbs*, 2001]. Stronger updrafts associated with lower glaciation temperatures maintain a high supersaturation with respect to liquid, offsetting the Bergeron-Findeisen process, therefore the glaciation process is delayed [*Korolev and Mazin*, 2003; *Korolev et al.*, 2017].

The global mean cloud feedback differences in models is associated with differences in the cloud phase feedback [*Zelinka et al.*, 2020]. *McCoy et al.* [2018] have shown that some global cloud models have liquid clouds at -53°C and some consider that clouds are ice at -13°C. The T_{50} retrieved in the present study, equal to -24°C, is lower than 19 of the global cloud models out of 26 analysed by *McCoy et al.* [2016], suggesting that global cloud model phase transition processes can be too efficient [*Komurcu et al.*, 2014; *Cesana et al.*, 2015; *Dietlicher et al.*, 2019]. The T_{50} retrieved in our study is also lower than the value retrieved by *Cesana et al.* [2015] and *Hu et al.* [2010] based on CALIPSO top phase observations but is higher than the value retrieved by *Westbrook and Illingworth* [2011] who show that 50% of clouds are in the ice phase at -27°C from ground based lidar and radar measurements. If the liquid dominated cloud fraction increases at the expense of ice dominated clouds, then because ice crystals tend to be relatively larger [*Zelinka et al.*, 2012; *McCoy et al.*, 2014] precipitation would be less efficient for a given amount of condensate [*Ceppi et al.*, 2016; *Mülmenstädt et al.*, 2015]. Therefore, the cloud lifetime and cloud feedback effects in numerical models would change. Our study can be used to help evaluate theories about cloud freezing temperature [*Cantrell and Heymsfield*, 2005; *Pinsky et al.*, 2018; *Phillips et al.*, 2018] and may help guide numerical models with partitioning of ice and liquid clouds and reduce uncertainty in the cloud phase feedback and climate sensitivity in global climate models [*Choi et al.*, 2014; *Tan et al.*, 2016].

Acknowledgments

ERA-Interim data can be downloaded from the website: http://www.ecmwf.int/en/research/climate-reanalysis/era-interim. MODIS and POLDER-3 data sets can be downloaded from ICARE:

©2020 American Geophysical Union. All rights reserved.

http://www.icare.univ-lille1.fr/archive?dir=PARASOL/PM-L2/. This project has received funding from the National Science Foundation under grant 1303965, the Department of Energy through award DE-SC0016282 and Université de Lille. The authors thank ICARE/AERIS Data and Services Center, NASA, and CNES for the data used in this research.

Accepted Article

©2020 American Geophysical Union. All rights reserved.

References

Barton, N. P., S. A. Klein, J. S. Boyle, and Y. Y. Zhang (2012), Arctic synoptic regimes: Comparing domain-wide Arctic cloud observations with CAM4 and CAM5 during similar dynamics, *Journal of Geophysical Research: Atmospheres*, *117*(D15), doi: 10.1029/2012JD017589.

Baum, B. A., W. P. Menzel, R. A. Frey, D. C. Tobin, R. E. Holz, S. A. Ackerman, A. K. Heidinger, and P. Yang (2012), MODIS Cloud-Top Property Refinements for Collection 6, *Journal of Applied Meteorology and Climatology*, *51*(6), 1145–1163, doi: 10.1175/JAMC-D-11-0203.1.

Berrisford, P., D. Dee, K. Fielding, M. Fuentes, P. Kallberg, S. Kobayashi, and S. Uppala (2011), The ERA-Interim Archive version 2.0, *Tech. rep.*, ECMWF, Reading, UK.

Bréon, F.-M., and S. Colzy (1999), Cloud Detection from the Spaceborne POLDER Instrument and Validation against Surface Synoptic Observations, *Journal of Applied Meteorology*, *38*(6), 777–785, doi:10.1175/1520-0450(1999)038<0777:CDFTSP>2.0.CO;2.

Buriez, J. C., C. Vanbauce, F. Parol, P. Goloub, M. Herman, B. Bonnel, Y. Fouquart, P. Couvert, and G. Seze (1997), Cloud detection and derivation of cloud properties from POLDER, *International Journal of Remote Sensing*, *18*(13), 2785–2813, doi: 10.1080/014311697217332.

Cantrell, W., and A. Heymsfield (2005), Production of Ice in Tropospheric Clouds: A Review, *Bulletin of the American Meteorological Society*, *86*(6), 795–808, doi: 10.1175/BAMS-86-6-795.

Carro-Calvo, L., C. Hoose, M. Stengel, and S. Salcedo-Sanz (2016), Cloud glaciation temperature estimation from passive remote sensing data with evolutionary computing, *Journal of Geophysical Research: Atmospheres*, *121*(22), 13,591–13,608, doi: 10.1002/2016JD025552.

Ceppi, P., D. L. Hartmann, and M. J. Webb (2016), Mechanisms of the Negative Shortwave Cloud Feedback in Middle to High Latitudes, *Journal of Climate*, *29*(1), 139–157, doi:10.1175/JCLI-D-15-0327.1.

Cesana, G., and H. Chepfer (2013), Evaluation of the cloud thermodynamic phase in a climate model using CALIPSO-GOCCP, *Journal of Geophysical Research: Atmospheres*, *118*(14), 7922–7937, doi:10.1002/jgrd.50376.

Cesana, G., D. E. Waliser, X. Jiang, and J. L. Li (2015), Multimodel evaluation of cloud phase transition using satellite and reanalysis data, *Journal of Geophysical Research*, *120*(15), 7871–7892, doi:10.1002/2014JD022932.

Choi, Y.-S., R. S. Lindzen, C.-H. Ho, and J. Kim (2010), Space observations of cold-cloud phase change, *Proceedings of the National Academy of Sciences*, *107*(25), 11,211–11,216, doi:10.1073/pnas.1006241107.

Choi, Y.-S., C.-H. Ho, C.-E. Park, T. Storelvmo, and I. Tan (2014), Influence of cloud phase composition on climate feedbacks, *Journal of Geophysical Research: Atmospheres*, *119*(7), 3687–3700, doi:10.1002/2013JD020582.

Chylek, P., S. Robinson, M. K. Dubey, M. D. King, Q. Fu, and W. B. Clodius (2006), Comparison of near-infrared and thermal infrared cloud phase detections, *Journal of Geophysical Research*, *111*(D20), D20,203, doi:10.1029/2006JD007140.

Coopman, Q., T. J. Garrett, J. Riedi, S. Eckhardt, and A. Stohl (2016), Effects of long-range aerosol transport on the microphysical properties of low-level liquid clouds in the Arctic, *Atmospheric Chemistry and Physics*, *16*(7), 4661–4674, doi:10.5194/acp-16-4661-2016.

Coopman, Q., J. Riedi, D. P. Finch, and T. J. Garrett (2018), Evidence for Changes in Arctic Cloud Phase Due to Long-Range Pollution Transport, *Geophysical Research Letters*, *45*(19), 10,709–10,718, doi:10.1029/2018GL079873.

Coopman, Q., C. Hoose, and M. Stengel (2019), Detection of Mixed Phase Convective Clouds by a Binary Phase Information From the Passive Geostationary Instrument SEVIRI, *Journal of Geophysical Research: Atmospheres*, *124*(9), 5045–5057, doi:

©2020 American Geophysical Union. All rights reserved.

10.1029/2018JD029772.

Dee, D. P., S. M. Uppala, a. J. Simmons, P. Berrisford, P. Poli, S. Kobayashi, U. Andrae, M. a. Balmaseda, G. Balsamo, P. Bauer, P. Bechtold, a. C. M. Beljaars, L. van de Berg, J. Bidlot, N. Bormann, C. Delsol, R. Dragani, M. Fuentes, a. J. Geer, L. Haimberger, S. B. Healy, H. Hersbach, E. V. Hólm, L. Isaksen, P. Kållberg, M. Köhler, M. Matricardi, A. P. McNally, B. M. Monge-Sanz, J.-J. Morcrette, B.-K. Park, C. Peubey, P. de Rosnay, C. Tavolato, J.-N. Thépaut, and F. Vitart (2011), The ERA-Interim reanalysis: configuration and performance of the data assimilation system, *Q. J. R. Meteorol. Soc.*, *137*(656), 553–597, doi:10.1002/qj.828.

Dietlicher, R., D. Neubauer, and U. Lohmann (2019), Elucidating ice formation pathways in the aerosolâĂŞclimate model ECHAM6-HAM2, *Atmospheric Chemistry and Physics*, *19*(14), 9061–9080, doi:10.5194/acp-19-9061-2019.

Doutriaux-Boucher, M., and J. Quaas (2004), Evaluation of cloud thermodynamic phase parametrizations in the LMDZ GCM by using POLDER satellite data, *Geophysical Research Letters*, *31*(6), doi:10.1029/2003GL019095.

Filioglou, M., T. Mielonen, D. Balis, E. Giannakaki, A. Arola, H. Kokkola, M. Komppula, and S. Romakkaniemi (2019), Aerosol Effect on the Cloud Phase of LowâĂŘLevel Clouds Over the Arctic, *Journal of Geophysical Research: Atmospheres*, *124*(14), 7886–7899, doi:10.1029/2018JD030088.

Goloub, P., M. Herman, H. Chepfer, J. Riedi, G. Brogniez, P. Couvert, and G. Séze (2000), Cloud thermodynamical phase classification from the POLDER spaceborne instrument, *Journal of Geophysical Research: Atmospheres*, *105*(D11), 14,747–14,759, doi:10.1029/1999JD901183.

Holz, R. E., S. A. Ackerman, F. W. Nagle, R. Frey, S. Dutcher, R. E. Kuehn, M. A. Vaughan, and B. Baum (2008), Global Moderate Resolution Imaging Spectroradiometer (MODIS) cloud detection and height evaluation using CALIOP, *Journal of Geophysical Research*, *113*(8), D00A19, doi:10.1029/2008JD009837.

Hu, Y., D. Winker, M. Vaughan, B. Lin, A. Omar, C. Trepte, and R. Holz (2009), CALIPSO/CALIOP Cloud Phase Discrimination Algorithm, *Journal of Atmospheric and Oceanic Technology*, *26*(11), 2293–2309, doi:10.1175/2009JTECHA1280.1.

Hu, Y., S. Rodier, K.-m. Xu, W. Sun, J. Huang, B. Lin, P. Zhai, and D. Josset (2010), Occurrence, liquid water content, and fraction of supercooled water clouds from combined CALIOP/IIR/MODIS measurements, *Journal of Geophysical Research*, *115*(19), D00H34, doi:10.1029/2009JD012384.

Jeffery, C. a., and P. H. Austin (1997), Homogeneous nucleation of supercooled water: Results from a new equation of state, *Journal of Geophysical Research: Atmospheres*, *102*(D21), 25,269–25,279, doi:10.1029/97JD02243.

Komurcu, M., T. Storelvmo, I. Tan, U. Lohmann, Y. Yun, J. E. Penner, Y. Wang, X. Liu, and T. Takemura (2014), Intercomparison of the cloud water phase among global climate models, *Journal of Geophysical Research: Atmospheres*, *119*(6), 3372–3400, doi:10.1002/2013JD021119.

Korolev, A., G. McFarquhar, P. R. Field, C. Franklin, P. Lawson, Z. Wang, E. Williams, S. J. Abel, D. Axisa, S. Borrmann, J. Crosier, J. Fugal, M. Krämer, U. Lohmann, O. Schlenczek, M. Schnaiter, and M. Wendisch (2017), Mixed-Phase Clouds: Progress and Challenges, *Meteorological Monographs*, *58*, 5.1–5.50, doi:10.1175/AMSMONOGRAPHS-D-17-0001.1.

Korolev, A. V., and I. P. Mazin (2003), Supersaturation of Water Vapor in Clouds, *J. Atmos. Sci.*, *60*, 2957–2974.

Matus, A. V., and T. S. L'Ecuyer (2017), The role of cloud phase in Earth's radiation budget, *Journal of Geophysical Research: Atmospheres*, *122*(5), 2559–2578, doi:10.1002/2016JD025951.

McCoy, D. T., D. L. Hartmann, and D. P. Grosvenor (2014), Observed Southern Ocean Cloud Properties and Shortwave Reflection. Part I: Calculation of SW Flux from Observed Cloud Properties, *Journal of Climate*, *27*(23), 8836–8857, doi:10.1175/JCLI-D-

©2020 American Geophysical Union. All rights reserved.

14-00287.1.

McCoy, D. T., I. Tan, D. L. Hartmann, M. D. Zelinka, and T. Storelvmo (2016), On the relationships among cloud cover, mixed-phase partitioning, and planetary albedo in GCMs, *Journal of Advances in Modeling Earth Systems*, *8*(2), 650–668, doi: 10.1002/2015MS000589.

McCoy, D. T., D. L. Hartmann, and M. D. Zelinka (2018), Mixed-Phase Cloud Feedbacks, in *Mixed-Phase Clouds*, edited by Elsevier, chap. 9, pp. 215–236, Elsevier, Amsterdam, doi:10.1016/B978-0-12-810549-8.00009-X.

McDonald, A. J., and S. Parsons (2018), A Comparison of Cloud Classification Methodologies: Differences Between Cloud and Dynamical Regimes, *Journal of Geophysical Research: Atmospheres*, *123*(19), 11,173–11,193, doi:10.1029/2018JD028595.

Mülmenstädt, J., O. Sourdeval, J. Delanoë, and J. Quaas (2015), Frequency of occurrence of rain from liquid-, mixed-, and ice-phase clouds derived from A-Train satellite retrievals, *Geophysical Research Letters*, *42*(15), 6502–6509, doi:10.1002/2015GL064604.

Nakajima, T., and M. D. King (1990), Determination of the Optical Thickness and Effective Particle Radius of Clouds from Reflected Solar Radiation Measurements. Part I: Theory, *Journal of the Atmospheric Sciences*, *47*(15), 1878–1893, doi:10.1175/1520-0469(1990)047<1878:DOTOTA>2.0.CO;2.

Phillips, V. T. J., S. Patade, J. Gutierrez, and A. Bansemer (2018), Secondary Ice Production by Fragmentation of Freezing Drops: Formulation and Theory, *Journal of the Atmospheric Sciences*, *75*(9), 3031–3070, doi:10.1175/JAS-D-17-0190.1.

Pilewskie, P., and S. Twomey (1987), Cloud Phase Discrimination by Reflectance Measurements near 1.6 and 2.2 μm, *Journal of the Atmospheric Sciences*, *44*(22), 3419–3420, doi:10.1175/1520-0469(1987)044<3419:CPDBRM>2.0.CO;2.

Pinsky, M., A. Khain, and A. Korolev (2018), Theoretical Analysis of LiquidâĂŞIce Interaction in the Unsaturated Environment with Application to the Problem of Homogeneous Mixing, *Journal of the Atmospheric Sciences*, *75*(4), 1045–1062, doi:10.1175/JAS-D-17-0228.1.

Platnick, S., R. Pincus, B. Wind, M. D. King, M. A. Gray, and P. Hubanks (2004), An initial analysis of the pixel-level uncertainties in global MODIS cloud optical thickness and effective particle size retrievals, *PROC. SPIE*, *5652*(December 2004), 30, doi: 10.1117/12.578353.

Platnick, S., M. D. King, K. G. Meyer, G. Wind, N. Amarasinghe, B. Marchant, G. T. Arnold, Z. Zhang, P. A. Hubanks, B. Ridgway, and J. Riedi (2014), MODIS Cloud Optical Properties: User Guide for the Collection 6 Level-2 MOD06/MYD06 Product and Associated Level-3 Datasets, *Tech. rep.*, NASA, Greenbelt.

Pruppacher, H. R. (1995), A New Look at Homogeneous Ice Nucleation in Supercooled Water Drops, *J. Atmos. Sci.*, *52*(11), 1924–1933, doi:10.1175/1520-0469(1995)052<1924:ANLAHI>2.0.CO;2.

Quaas, J. (2012), Evaluating the "critical relative humidity" as a measure of subgrid-scale variability of humidity in general circulation model cloud cover parameterizations using satellite data, *Journal of Geophysical Research: Atmospheres*, *117*(D9), doi: 10.1029/2012JD017495.

Rangno, A. L., and P. V. Hobbs (2001), Ice particles in stratiform clouds in the Arctic and possible mechanisms for the production of high ice concentrations, *J. Geophys. Res. Atmos.*, *106*(D14), 15,065–15,075, doi:10.1029/2000JD900286.

Riedi, J., B. Marchant, S. Platnick, B. A. Baum, F. Thieuleux, C. Oudard, F. Parol, J.-M. Nicolas, and P. Dubuisson (2010), Cloud thermodynamic phase inferred from merged POLDER and MODIS data, *Atmospheric Chemistry and Physics*, *10*(23), 11,851–11,865, doi:10.5194/acp-10-11851-2010.

Rosenfeld, D., X. Yu, G. Liu, X. Xu, Y. Zhu, Z. Yue, J. Dai, Z. Dong, Y. Dong, and Y. Peng (2011), Glaciation temperatures of convective clouds ingesting desert dust, air pollution and smoke from forest fires, *Geophysical Research Letters*, *38*(21), L21,804, doi:10.1029/2011GL049423.

©2020 American Geophysical Union. All rights reserved.

Tan, I., T. Storelvmo, and M. D. Zelinka (2016), Observational constraints on mixed-phase clouds imply higher climate sensitivity, *Science*, *352*(6282), 224–227, doi:10.1126/science.aad5300.

Tapiador, F. J., A. Navarro, A. Jiménez, R. Moreno, and E. GarcíaâĂŘOrtega (2018), Discrepancies with satellite observations in the spatial structure of global precipitation as derived from global climate models, *Quarterly Journal of the Royal Meteorological Society*, *144*(S1), 419–435, doi:10.1002/qj.3289.

Taylor, P. C., S. Kato, K.-M. Xu, and M. Cai (2015), Covariance between Arctic sea ice and clouds within atmospheric state regimes at the satellite footprint level, *Journal of Geophysical Research: Atmospheres*, *120*(24), 12,656–12,678, doi:10.1002/2015JD023520.

Westbrook, C. D., and A. J. Illingworth (2011), Evidence that ice forms primarily in supercooled liquid clouds at temperatures > -27C, *Geophysical Research Letters*, *38*(14), doi:10.1029/2011GL048021.

Winker, D. M., M. a. Vaughan, A. Omar, Y. Hu, K. a. Powell, Z. Liu, W. H. Hunt, and S. a. Young (2009), Overview of the CALIPSO mission and CALIOP data processing algorithms, *J. Atmos. Ocean. Technol.*, *26*(11), 2310–2323, doi:10.1175/2009JTECHA1281.1.

Zelinka, M. D., S. A. Klein, and D. L. Hartmann (2012), Computing and Partitioning Cloud Feedbacks Using Cloud Property Histograms. Part II: Attribution to Changes in Cloud Amount, Altitude, and Optical Depth, *Journal of Climate*, *25*(11), 3736–3754, doi:10.1175/JCLI-D-11-00249.1.

Zelinka, M. D., T. A. Myers, D. T. McCoy, S. PoâĂŘChedley, P. M. Caldwell, P. Ceppi, S. A. Klein, and K. E. Taylor (2020), Causes of Higher Climate Sensitivity in CMIP6 Models, *Geophysical Research Letters*, *47*(1), 1–12, doi:10.1029/2019GL085782.

Accepted Article

©2020 American Geophysical Union. All rights reserved.

Table 1. Values considered to define the different bins of r_e^{Liq}, latitude, ω_{700}, and SH^a_{700}.

r_e^{Liq} (μm)	Latitudes (°)	ω_{700} (Pa/s)	SH_{700} (g/kg)
5	-90	-1.0	0.0
9	-60	-0.8	0.3
13	-30	-0.6	0.6
17	0	-0.4	1.1
21	30	-0.2	2.5
25	60	0.0	15.6
	90	5.0	

[a]The values to determine SH_{700} are based on the 0^{th}, 20^{th}, 40^{th}, 60^{th}, 80^{th}, and 100^{th} percentiles.

Figure 1. Cloud top phase (Φ) distribution from the algorithm developed by *Riedi et al.* [2010]. The vertical bars for confident liquid, liquid, ice, and confident ice are respectively at Φ equal to 20, 60, 140, and 180.

Figure 2. (a) Cumulative distribution function (CDF) of liquid cloud top temperatures (CDF(liquid)) in red and 1- CDF(ice) in blue for two degrees of confidence in the phase index (Φ). (b) Fraction of CDF(ice) defined as $\frac{1-CDF(ice)}{1-CDF(ice)+CDF(liq)}$ considering two levels of confidence in Φ (purple) and the hyperbolic tangential fit retrieved from the fraction of CDF(ice) and T_{50} is retrieved from Equation (2). (c) T_{50} is retrieved considering all the pixels, for different bins of latitude, and surface type. The diamonds consider a higher confidence in the phase retrieval than the dots. The squares show the average between T_{50} retrieved considering the high and low level of confidence in the phase detection for each regime considered.

Accepted Article

©2020 American Geophysical Union. All rights reserved.

Accepted Article

Figure 3. Glaciation temperature T_{50} from Equation (2) for different cloud droplet effective radius bins considering global data. The diamonds on the dashed line consider a higher confidence in the phase retrieval — Phase index (Φ) less than 20 for liquid cloud detection and Φ greater than 180 for ice cloud detection — than the dots on the solid line — Φ less than 60 for liquid cloud detection and Φ greater than 140 for ice cloud detection. The results from the dashed lines are supported by fewer data points but the phase determination is more robust than the results shown by the solid line. The area between the solid and the dashed lines represent an estimate of the uncertainty introduced by the phase decision itself.

Figure 4. Glaciation temperature T_{50} from Equation (2) for different bins of cloud droplet effective radius, and latitude (a, b, c), large-scale pressure velocity (d, e, f), and specific humidity (g, h, i). Global data are considered for the bins of large-scale pressure velocity and specific humidity. The diamonds on the dashed line consider a higher confidence in the phase retrieval — Phase index (Φ) less than 20 for liquid cloud detection and Φ greater than 180 for ice cloud detection — than the dots on the solid line — Φ less than 60 for liquid cloud detection and Φ greater than 140 for ice cloud detection. The hatched area represents the uncertainty.

©2020 American Geophysical Union. All rights reserved.

Figure 1.

Accepted Article

©2020 American Geophysical Union. All rights reserved.

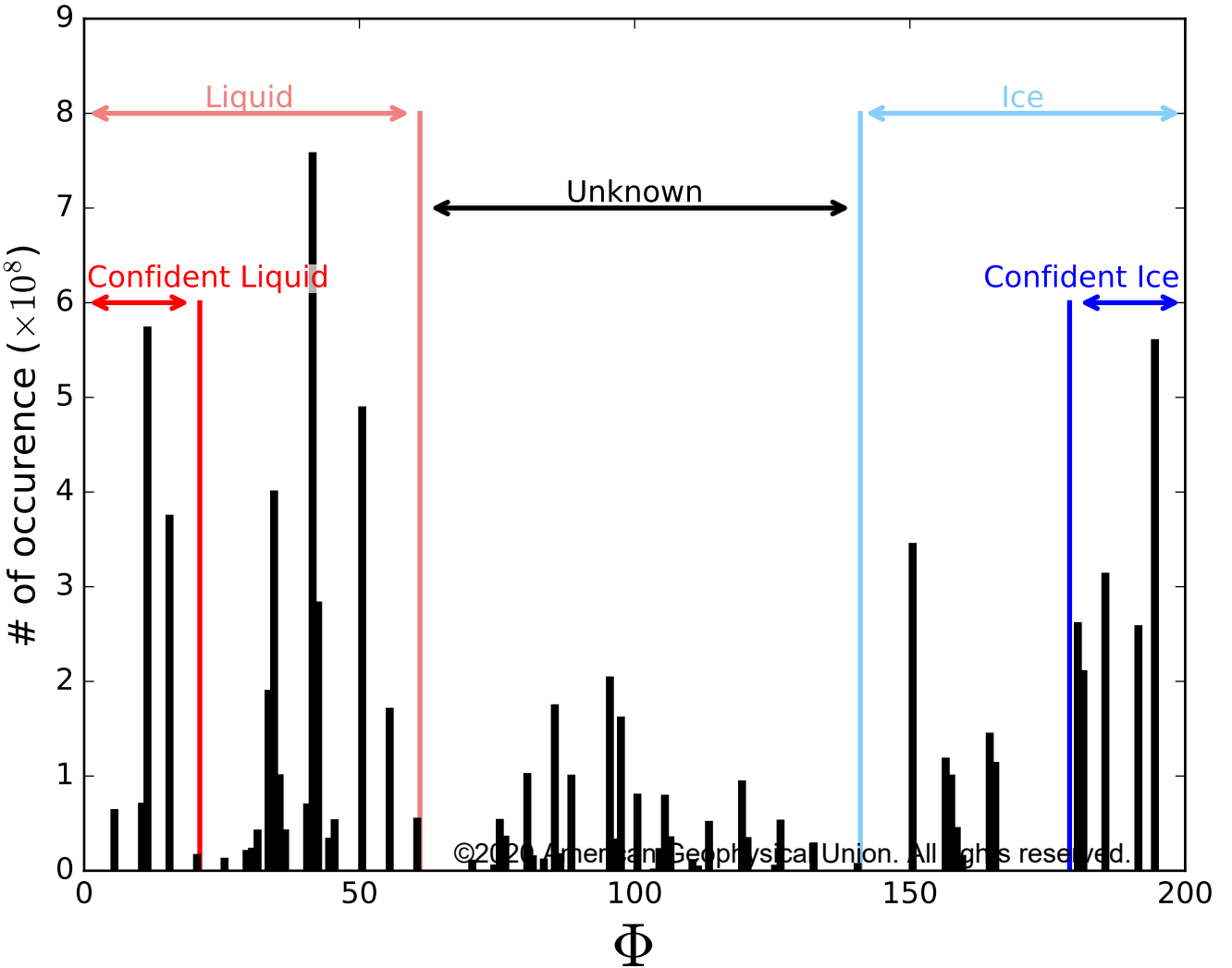
Liquid
Ice
Unknown
Confident Liquid
Confident Ice
# of occurence ($\times 10^8$)
Φ
0
1
2
3
4
5
6
7
8
9
0
50
100
150
200
©2020 American Geophysical Union. All rights reserved.

Figure 2.

Accepted Article

©2020 American Geophysical Union. All rights reserved.

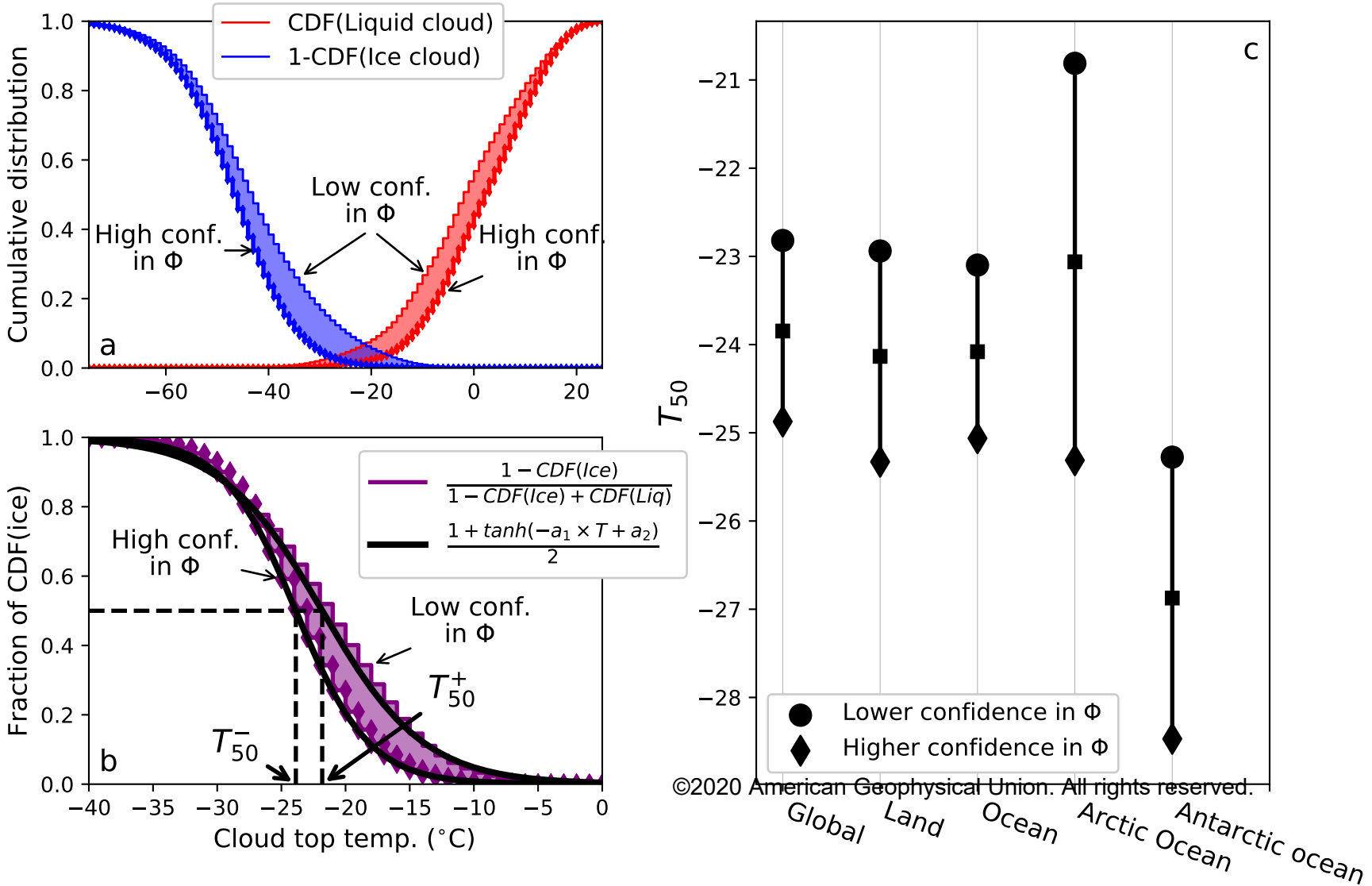

©2020 American Geophysical Union. All rights reserved.

Figure 3.

Accepted Article

©2020 American Geophysical Union. All rights reserved.

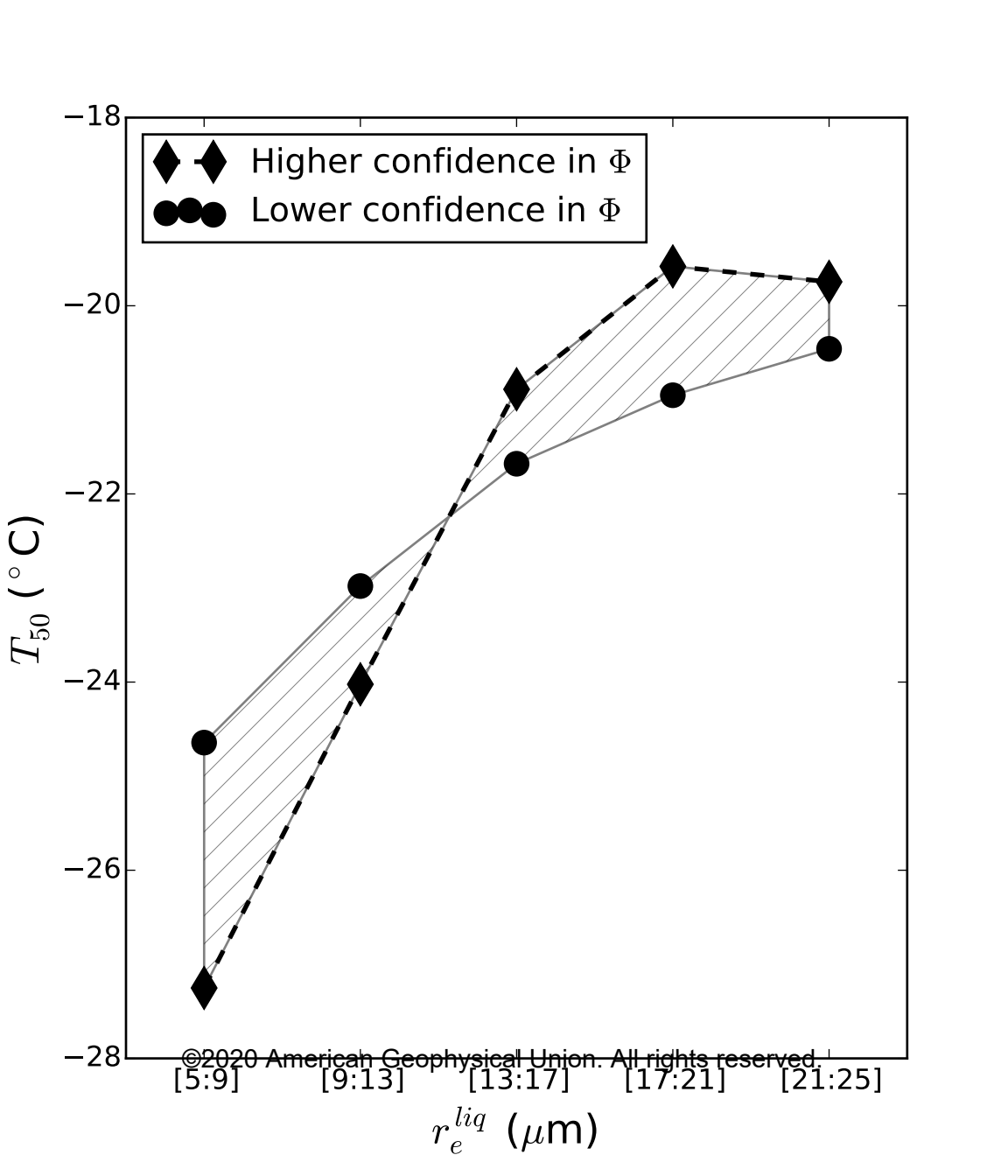

©2020 American Geophysical Union. All rights reserved.

Figure 4.

Accepted Article

©2020 American Geophysical Union. All rights reserved.

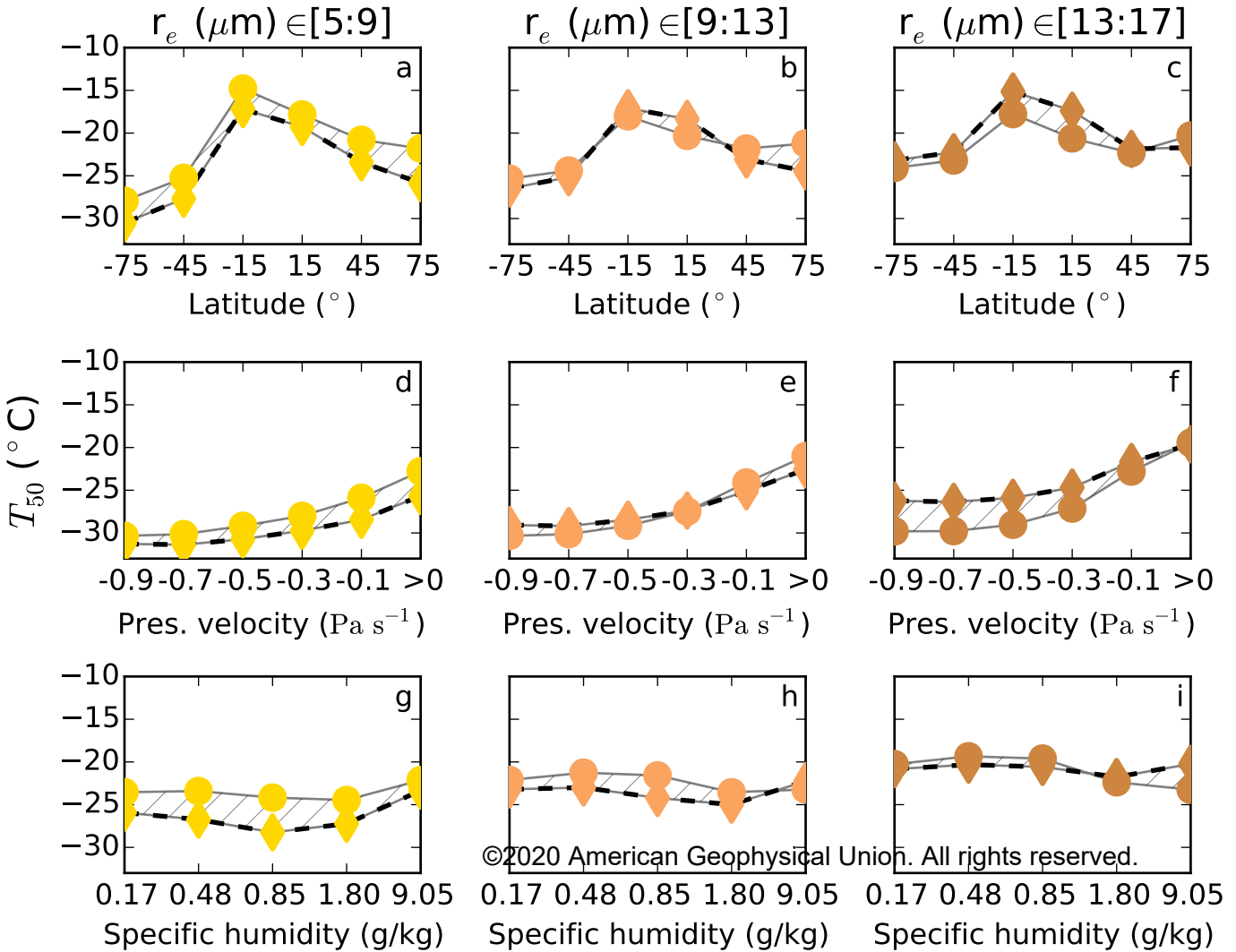

©2020 American Geophysical Union. All rights reserved.